Available online at www.sciencedirect.com

ScienceDirect

Advances in Space Research 63 (2019) 270–281

ADVANCES IN SPACE RESEARCH (a COSPAR publication)

www.elsevier.com/locate/asr

Multi-instrument observations of large-scale atmospheric gravity waves/traveling ionospheric disturbances associated with enhanced auroral activity over Svalbard

Zama T. Katamzi-Joseph [a,b,*], Anasuya L. Aruliah [c], Kjellmar Oksavik [d,e], John Bosco Habarulema [a,b], Kirsti Kauristie [f], Michael J. Kosch [a,g,h]

[a] SANSA Space Science, Hermanus, South Africa
[b] Dept. Physics & Electronics, Rhodes University, Grahamstown, South Africa
[c] Dept. Physics & Astronomy, University College London, London, UK
[d] Birkeland Centre for Space Science, Dept. Physics & Technology, University of Bergen, Bergen, Norway
[e] Arctic Geophysics, University Centre in Svalbard, Longyearbyen, Norway
[f] Finnish Meteorologica Institute, Helsinki, Finland
[g] Dept. Physics, Lancaster University, Lancaster, UK
[h] Dept. Physics & Astronomy, University of the Western Cape, Bellville, South Africa

Received 30 April 2018; received in revised form 24 August 2018; accepted 27 August 2018
Available online 3 September 2018

Abstract

This study reports on observations of large-scale atmospheric gravity waves/traveling ionospheric disturbances (AGWs/TIDs) using Global Positioning System (GPS) total electron content (TEC) and Fabry–Perot Interferometer's (FPI's) intensity of oxygen red line emission at 630 nm measurements over Svalbard on the night of 6 January 2014. TEC large-scale TIDs have primary periods ranging between 29 and 65 min and propagate at a mean horizontal velocity of ~749–761 m/s with azimuth of ~345–347° (which corresponds to poleward propagation direction). On the other hand, FPI large-scale AGWs have larger periods of ~42–142 min. These large-scale AGWs/TIDs were linked to enhanced auroral activity identified from co-located all-sky camera and IMAGE magnetometers. Similar periods, speed and poleward propagation were found for the all-sky camera (~60–97 min and ~823 m/s) and the IMAGE magnetometers (~32–53 min and ~708 m/s) observations. Joule heating or/and particle precipitation as a result of auroral energy injection were identified as likely generation mechanisms for these disturbances.

Keywords: Atmospheric gravity waves; Traveling ionospheric disturbances; Substorm; Aurora; Arctic polar cap; ANGWIN

1. Introduction

Atmospheric gravity waves (AGWs) have been well studied for over five decades since the advent of the pioneering work by Hines (1960). Traveling ionospheric disturbances (TIDs) are signatures of AGWs in the ionosphere. AGWs/TIDs appear as wave-like perturbations in the atmospheric/thermospheric/ionospheric measurements, such as temperature, wind, plasma density and electron

* Corresponding author at: SANSA Space Science, Hermanus, South Africa.
E-mail addresses: zkatamzi@sansa.org.za (Z.T. Katamzi-Joseph), anasuya@star.ucl.ac.uk (A.L. Aruliah), Kjellmar.Oksavik@uib.no (K. Oksavik), jhabarulema@sansa.org.za (J.B. Habarulema), Kirsti.Kauristie@fmi.fi (K. Kauristie), mkosch@sansa.org.za (M.J. Kosch).

https://doi.org/10.1016/j.asr.2018.08.042
0273-1177/

concentration. These perturbations may be generated in the lower atmosphere (through processes such as mountain wave breaking, weather fronts, deep convection, etc) and propagate to the upper atmosphere where they eventually dissipate and may even generate secondary/tertiary waves (e.g. Balachandran, 1980; Gall et al., 1988; Taylor and Hapgood, 1988; Fovell et al., 1992; Fritts and Nastrom, 1992; Satomura and Sato, 1999; Vadas and Liu, 2009; Becker and Vadas, 2018; Vadas et al., 2018). Alternatively, they may be generated in the upper atmosphere by an energy input from the magnetosphere during a magnetic substorm or storm activity (e.g. Chan and Villard, 1962; Davis, 1971; Rees et al., 1984; Hajkowicz and Hunsucker, 1987; Hajkowicz, 1990; Hocke and Schlegel, 1996; Tsugawa et al., 2003; Ding et al., 2008; Katamzi and Habarulema, 2014; Borries et al., 2016; Pradipta et al., 2016; Zakharenkova et al., 2016; Figueiredo et al., 2017; Habarulema et al., 2018). Therefore, AGWs/TIDs are seen as a dynamical process that transport energy between different atmospheric and latitude regions, and as a result it is important to understand their properties and behaviour. In addition, since AGWs/TIDs can be accompanied by plasma instabilities that cause localised ionospheric irregularities (e.g. plasma bubbles), which can dramatically affect satellite-based navigation systems (Hernàndez-Parajes et al., 2006; Nishioka et al., 2009; Datta-Barua et al., 2010; Yoon and Lee, 2014; Takahashi et al., 2018), improving our understanding on AGWs/TIDs characteristics and their triggers can be useful for space weather applications.

AGWs/TIDs are commonly classified into two main groups: medium-scale and large-scale. Medium-scale AGWs/TIDs have relatively short period of 15–60 min, horizontal speeds and wavelengths of 100–250 m/s and less than ~100 to 400 km, respectively, (Mayr et al., 1984). However, more modern studies have extended medium-scale TIDs' horizontal wavelengths to 1000 km (Kotake et al., 2007) and even 1500 km (Otsuka et al., 2013; Figueiredo et al., 2018). The medium-scale TIDs are observed almost all the time and are mostly associated with meteorological phenomena, such as solar terminators, eclipses, etc. (Hernàndez-Parajes et al., 2006). Large-scale AGWs/TIDs have periods larger than 30 min, wavelengths longer than 1000 km, and horizontal propagation speeds larger than 400 m/s (Afraimovich et al., 2000; Ding et al., 2007; Afraimovich et al., 2013; Habarulema et al., 2018). These disturbances are largely associated with disturbed magnetic conditions, but not exclusively (Ding et al., 2008).

Past investigations of large-scale AGWs/TIDs linked to geomagnetic disturbances, in particular geomagnetic storms, have largely focused on middle and low latitude events (e.g. Hajkowicz and Hunsucker, 1987; Shiokawa et al., 2002; Lee et al., 2004; Hayashi et al., 2010; Ngwira et al., 2012; Katamzi and Habarulema, 2014; Habarulema et al., 2015; Borries et al., 2016; Figueiredo et al., 2017). Even after the advent of Global Navigation Satellite System (GNSS), especially Global Positioning System (GPS), there has been very little work that combines optical and radio data to study the characteristics of AGWs/TIDs, particularly in the polar regions and during auroral disturbances. However, some polar AGWs/TIDs studies have been conducted using either optical data like airglow imagers/cameras (e.g. Viereck and Deehr, 1989; Innis et al., 2001; Matsuda et al., 2017) or FPI (e.g. Ford et al., 2006, 2008; Nicolls et al., 2012; Shiokawa et al., 2012) or satellite data (e.g. Johnson et al., 1995; Idrus et al., 2013; Momani et al., 2010) or data from radars such as ionosondes and EISCAT (European Incoherent SCATter) (e.g. MacDougall et al., 1997; Cai et al., 2011; Vlasov et al., 2011). In particular, there are very few reported large-scale AGWs/TIDs observations from FPI measurements. For example, using a combination of instruments including incoherent scatter radars and FPIs over North America and Greenland, Pi et al. (2000) reported on large-scale TIDs induced by auroral heating effects during moderate storm and substorm activities on 27–28 October 1992. Shiokawa et al. (2003) utilised measurements from a suite of instruments including an FPI at low and midlatitudes in Japan, and reported observations of equatorward large-scale TIDs caused by intense poleward winds in the lower thermosphere (90–100 km) associated with an intense storm-time substorm on 31 March 2001. Employing FPIs located in northern Scandinavia, Ford et al. (2006) also observed large-scale AGWs during a tristatic campaign of 25 November 2003; although not specifically classified as a large-scale AGWs in that paper, but their reported characteristics match those of large-scale AGWs/TIDs. In a subsequent climatological study, Ford et al. (2008) reported on medium-scale and large-scale AGWs using FPIs in Sweden, Finland and Svalbard during the period of 2000–2006. They found no statistical difference between solar minimum and solar maximum as well as between different geomagnetic activity levels in the number of nighttime AGWs observed. Using a FPI located in Poker Flat, Nicolls et al. (2012) reported on AGWs activity during a period of enhanced auroral activity on 9–10 January 2010. These AGWs had period, velocity and wavelength characteristics matching those in the large-scale category.

Contrary to the high latitude case, there have been many studies of AGWs/TIDs observed at lower latitudes and directly linking them to auroral sources. For examples, Davis (1971) reported that it was possible to show a connection between the occurrences of TIDs and substorms on a one-to-one basis using TEC measurements from midlatitude stations and magnetometer stations in the northern hemisphere high-latitudes. Using measurements from ionosondes, riometers and magnetometers, Hajkowicz and Hunsucker (1987) presented evidence that auroral particle precipitation at the start of intense geomagnetic substorms can be associated with the launching of large-scale TIDs observed at middle and low latitudes. More recently, Shiokawa et al. (2002) presented characteristics of a large-scale TID observed over midlatitude Japan from a combination of all-sky imagers, GPS and ionosondes data during

a storm on 15 September 1999. They used the Sheffield University Plasmaspheric-Ionosphere Model (SUPIM), magnetic field measurements from magnetometers and UV auroral images from the Polar UVI instrument to link this disturbance to an intense auroral energy input which caused enhanced poleward neutral winds which in turn triggered the TID.

This paper reports on large-scale AGWs/TIDs observed on the night of 6 January 2014 over Svalbard, which is located in the Arctic polar cap. A combination of TEC and intensity of the 630 nm red line emission measurements were used to determine the period and propagation characteristics of the AGWs/TIDs. In addition, we analysed auroral activity using an all-sky camera and several magnetometers to determine the origin and generation mechanisms of the observed AGWs/TIDs.

2. Instrumentation and data

Measurements used to study the AGWs/TIDs and to investigate their possible origin were obtained from GNSS receivers, **FPI**, an all-sky camera and magnetometers in the Svalbard archipelago, namely in Spitsbergen, Hopen and Bear Island. The location of these instruments are shown in the map given in Fig. 1(a). In addition, coordinates of these instruments are given in Table 1.

The TEC data in this study were calculated from GPS L1 (1575.42 MHz) and L2 (1227.60 MHz) signals at 60 s cadence. This data were collected by a set of multi-constellation NovAtel GPStation-6 receivers (NovAtel Inc., 2012) that the University of Bergen installed in Svalbard in 2013. Data from these receivers have been used in the past to study the poleward edge of the nightside auroral oval (van der Meeren et al., 2015), dayside auroral forms (Oksavik et al., 2015), and polar cap arcs (van der Meeren et al., 2016). Fig. 1(b) shows projections of ionospheric pierce points (IPPs), calculated assuming the ionosphere is a thin shell sitting at 300 km, for satellites with elevation angles greater than 30° to illustrate our TEC data spatial coverage.

Intensities of the atomic oxygen red line emission at 630 nm measured at ~9 min cadence by the FPI in Longyearbyen were also used in this study. The FPI, owned by University College London, has a field of view of 1° at an elevation angle of 30°. More information on this instrument can be found from Aruliah and Griffin (2001), and references therein. During the night of interest the FPI was observing in five look directions, namely north-east

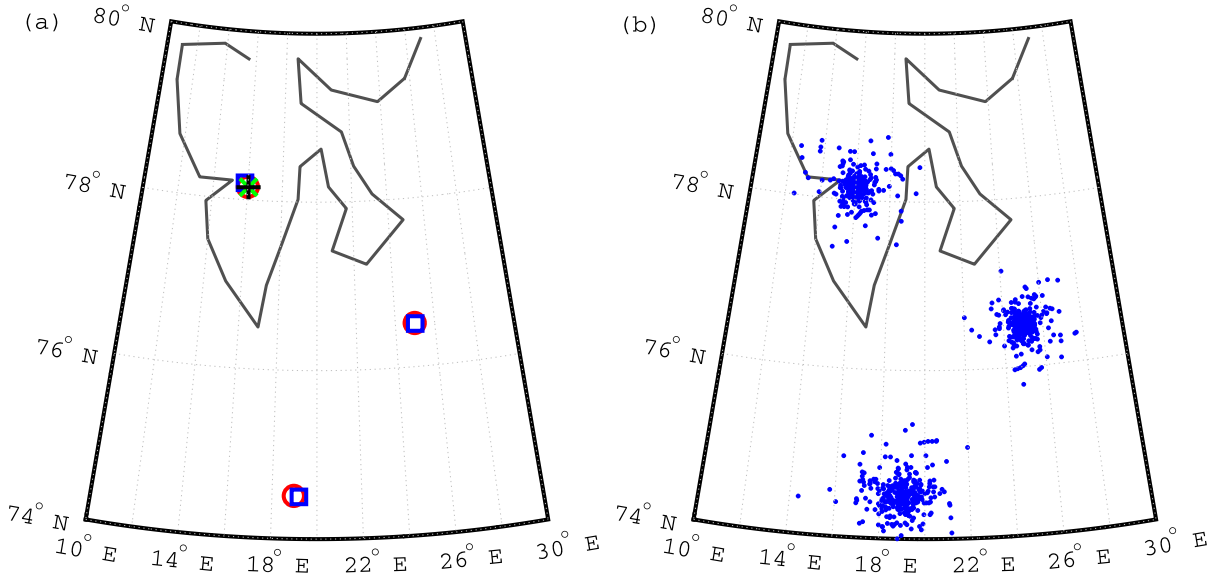

Fig. 1. Maps showing: (a) locations of GNSS receivers (blue squares), FPI (green cross), all-sky camera (black plus sign) and magnetometers (red circle) used in this study; (b) ionospheric pierce points for GPS PRNs 3, 6 and 11. (For interpretation of the references to colour in this figure legend, the reader is referred to the web version of this article.)

Table 1
Geographic and corrected geomagnetic coordinates, in degrees, of instruments used in this study. North and East are denoted by positive latitude and longitude values, respectively.

Station code	Geographic latitude	Geographic longitude	Magnetic latitude	Magnetic longitude
BJN[a]	74.51	19.00	71.76	106.29
HOP[a]	76.51	25.01	73.44	113.50
KHO/LYR[b]	78.15	16.04	75.52	109.93

[a] GNSS and magnetometer.
[b] GNSS, FPI, magnetometer and all-sky camera.

(NE), north-west (NW), south-east (SE), south-west (SW) and zenith (ZEN). In addition, intensity keogram of 557.7 nm airglow, in 1 min cadence, from an all-sky camera (ASC) operating in Longyearbyen was used for this study. More information on this type of instrument, which is part of the Magnetometer Ionospheric Radars All-sky Large Experiment (MIRACLE) network operated by the Finnish Meteorological Institute (FMI), can be found in Sangalli et al. (2011). Lastly, measurements of the X-component of the magnetic field from the International Monitor for Auroral Geomagnetic Effects (IMAGE) magnetometers co-located with the GPS receivers were also used to determine the influence of the auroral magnetic disturbance on observed AGWs/TIDs. More information on the IMAGE magnetometer network can be found in Guo et al. (2014).

3. Results

Fig. 2 shows auroral electrojet indices, i.e. AU, AL and AE, as well as the polar cap index on 6–7 January 2014. The auroral electrojet indices, first introduced by Davis and Sugiura (1966), are widely used as a measure of high-latitude magnetic activity, in particular substorm-related activity (Vennerstrøm et al., 1991). The polar cap index, instituted by Troshichev and Andrezen (1985), is derived from the Thule/Qaanaaq ground-based magnetometer and describes the geomagnetic disturbances related to the solar wind conditions in the northern polar region (Vaasiliadis et al., 1996; Stauning, 2013). From Fig. 2 a few minor geomagnetic disturbances were observed to have occurred throughout this night, and especially around 18 UT when TIDs (i.e. wavelike structures) were also observed as shown in Fig. 3. Fig. 3 presents TEC and TEC perturbations (DTEC) between 16 and 22 UT on 6 January 2014 for GPS satellites with pseudorandom noise

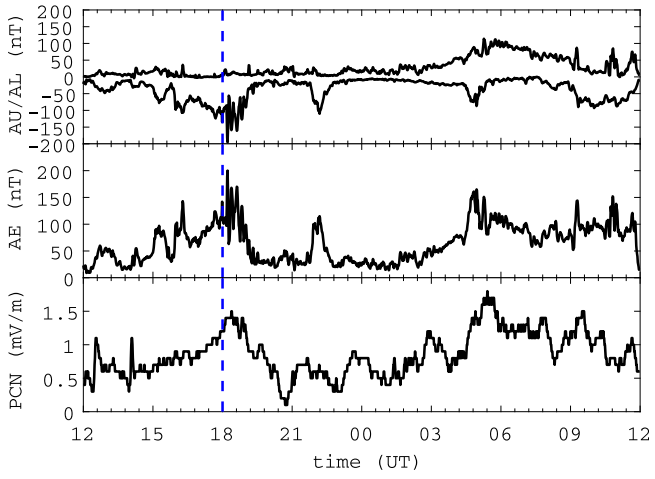

Fig. 2. Auroral electrojet indices: AU and AL (top panel), AE (middle panel) and polar cap index from Thule/Qaanaaq (PCN) (bottom panel) on 6–7 January 2014. The vertical blue dash line roughly indicates occurrence of disturbances in the GPS, FPI, ASC and magnetometer measurements. (For interpretation of the references to colour in this figure legend, the reader is referred to the web version of this article.)

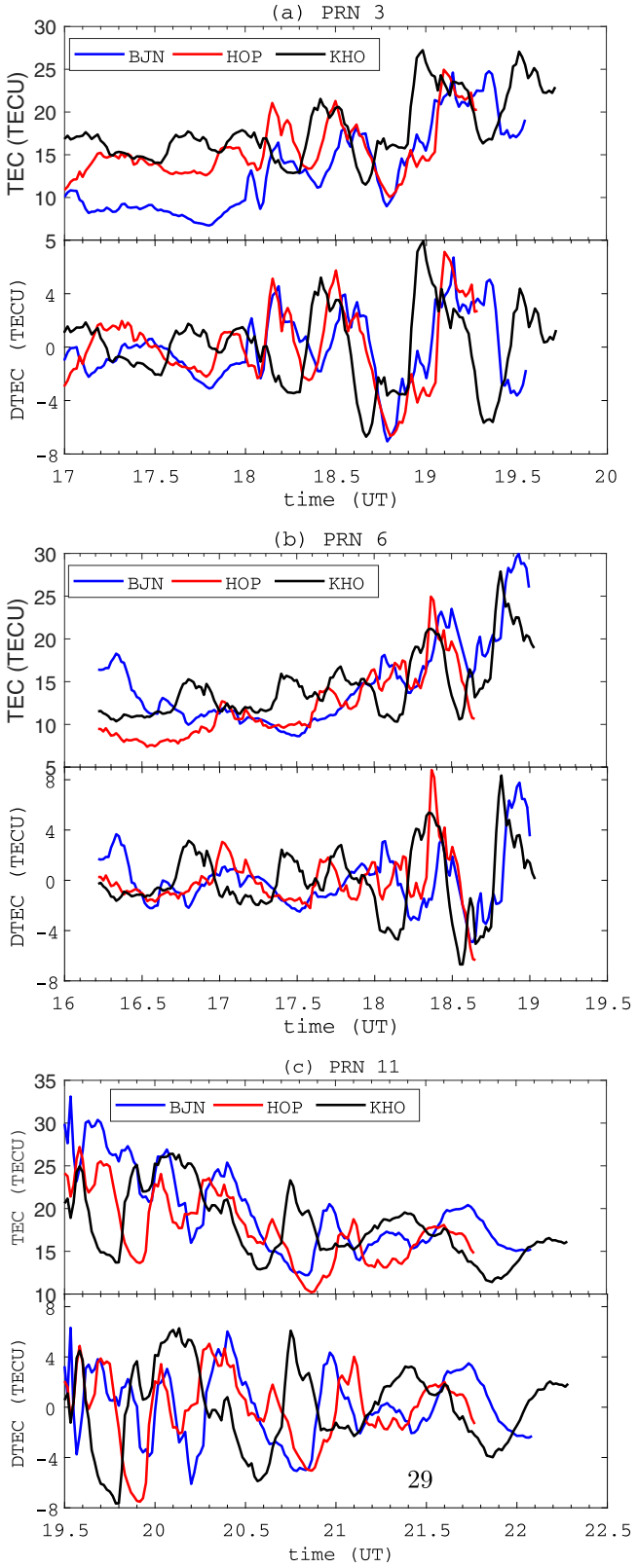

Fig. 3. TEC and TEC perturbations (top and bottom panels respectively) observed with GPS PRNs (a) 3, (b) 6, and (c) 11 on 6 January 2014.

(PRN) numbers 3, 6 and 11 observed at BJN, HOP and KHO. Although wavelike structures are also observed in measurements from PRNs 9, 18, 19 and 28, they are not

as clearly defined as those in PRNs 3, 6 and 11 even when the background TEC is removed. TEC perturbations were determined from removing the diurnal variation, which was estimated by a fourth order polynomial, similar to Valladares et al. (2009), Habarulema et al. (2016).

In order to estimate the periods of these TIDs we used Lomb-Scargle least squares frequency analysis of unevenly spaced data (Lomb, 1976; Scargle, 1982), and the results are shown in Fig. 4. From this figure it is observed that the dominating periods (i.e. above 75% confidence level) vary across PRNs and slightly at different observing stations. For example, from Fig. 4(a) the primary periods (above 99.99% confidence level) are 29 (KHO), 32 (BJN), 37 (HOP and KHO), and 58 min (BJN and HOP). Similarly Fig. 4(b) shows that the primary modes observed from PRN 6 measurements are 29 (KHO), 43 (HOP) and 46 min (BJN and KHO). Lastly PRN 11 detected TIDs with primary period of 39 min (BJN and KHO) as seen from Fig. 4(c). Note that period peaks that are too wide, i.e. half maximum full width larger than 30 min (roughly the minimum primary mode detected), are ignored to minimise ambiguity in determining the dominant periods. In addition several secondary modes (confidence level above 75% but below 99.99%) are also detected and these have periods ranging between 14 and 65 min. Note that all dominant periods detected from the GPS TEC are detailed in Table 2. Using the statistical angle of arrival and Doppler method for GPS radio interferometry (SADM-GPS), first introduced by Afraimovich et al. (1998) and also used by Valladares and Hei (2012) and Habarulema et al. (2013), we found that these TIDs were propagating with velocities of approximately 760 ± 235, 761 ± 258, and 749 ± 267 m/s as well as azimuths of about 347° ± 19°, 346° ± 22°, and 345° ± 20° (measured clockwise from north) for waves detected by PRNs 3, 6, and 11, respectively. These properties match the characteristics of large-scale TIDs (e.g. Hocke and Schlegel, 1996).

Table 2
Dominant periods of TIDs detected from GPS TEC measurements.

Mode	Station	Periods (minutes)
	PRN 3	
Primary	BJN	32, 58
	HOP	37, 58
	KHO	29, 37
Secondary	HOP	19, 28
	KHO	65
	PRN 6	
Primary	BJN	46
	HOP	43
	KHO	46, 29
Secondary	BJN	18, 22, 26, 33
	HOP	14, 22
	PRN 11	
Primary	BJN	39
	KHO	39
Secondary	BJN	18
	HOP	21, 28
	KHO	25

Fig. 5(a) and (i) show intensity and wind measurements of the oxygen 630 nm in several look directions taken using

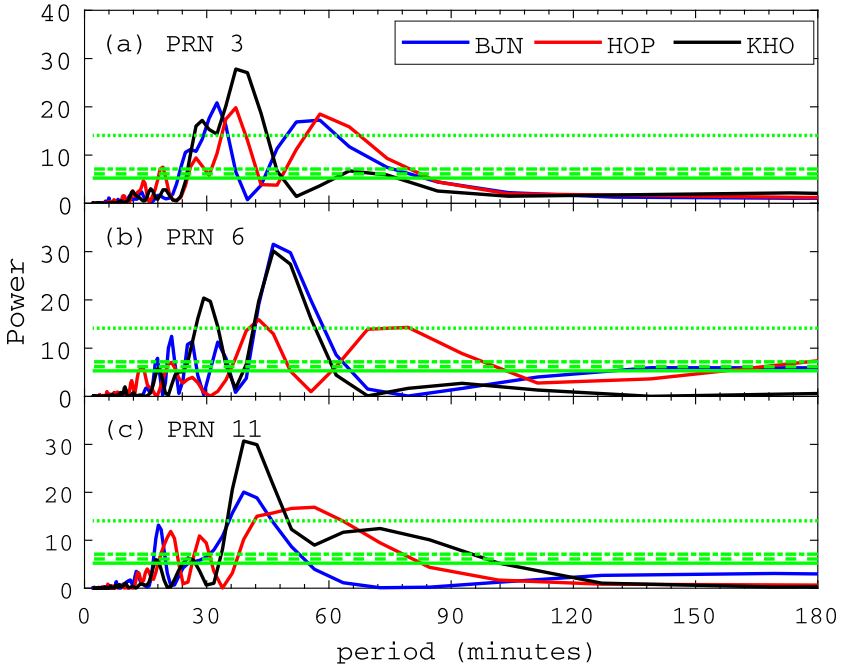

Fig. 4. Periodograms of the DTEC results shown in Fig. 3. The green horizontal lines show confidence levels of 99.99% (dotted line), 90% (dot-dash line), 75% (dash line), and 50% (solid line). (For interpretation of the references to colour in this figure legend, the reader is referred to the web version of this article.)

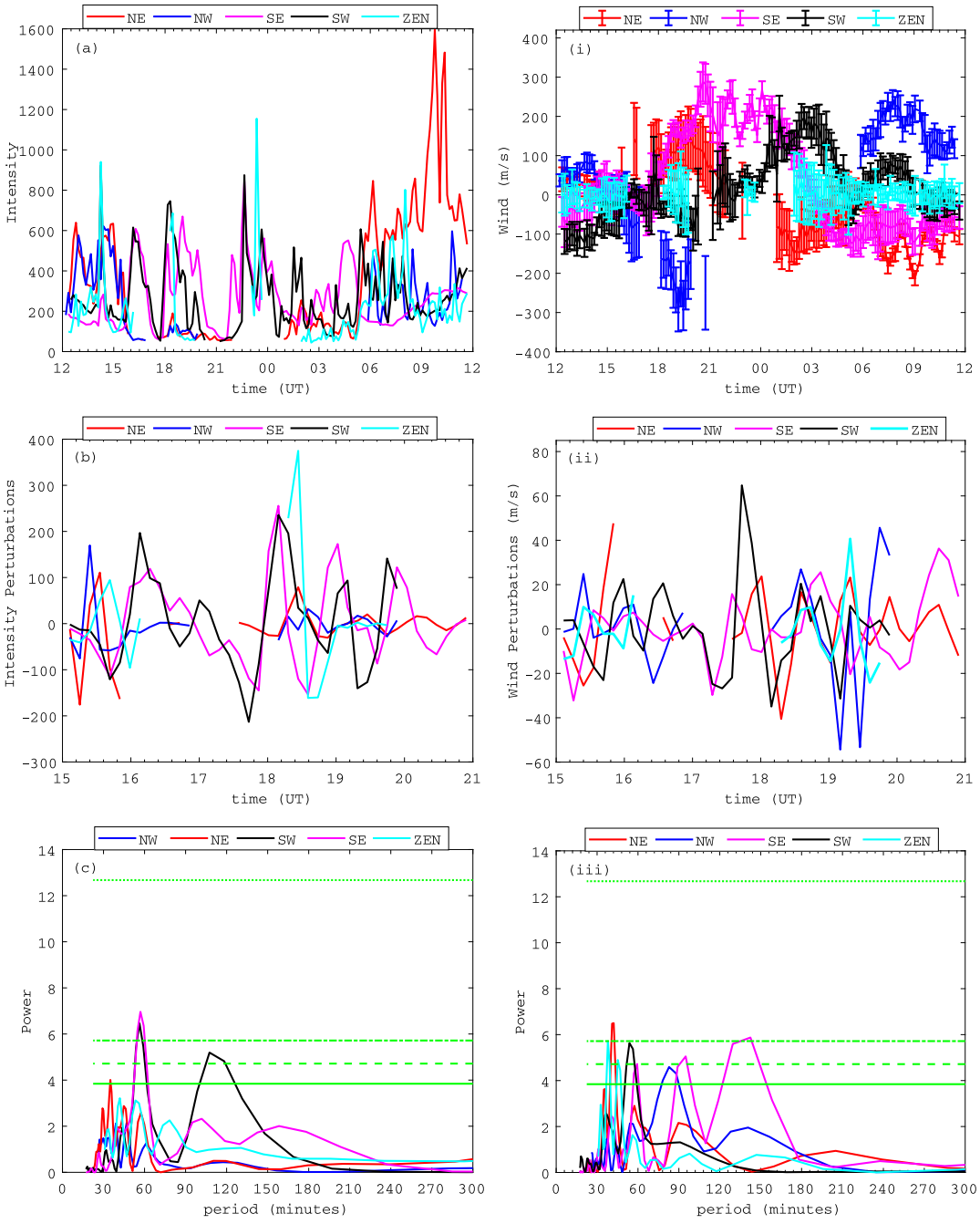

Fig. 5. Variations of intensities (a) and winds(i) of 630 nm from the FPI in Longyearbyen on 6–7 January 2014. Perturbations in intensity and wind measurements (b and (ii) respectively) between 15 and 21 UT as well as their respective periodograms (c and iii). The green horizontal lines show the same confidence levels as in Fig. 4. (For interpretation of the references to colour in this figure legend, the reader is referred to the web version of this article.)

an FPI in Longyearbyen. Although there are data gaps in some look directions during the time when TIDs were identified from the GPS data, the intensities in the SE and SW look directions show periodic increases between 15 and 00 UT. However similar wave-like variations are not as prominent in the wind speed data, although an enhancement in the SE and SW winds is observed from around 18 UT, i.e. same time as disturbances are observed in geomagnetic indices as well as GPS data. In order to highlight intensity and wind perturbations and therefore extract AGWs/TIDs characteristics, data between 15 and 21 UT were smoothed using a running 60 min mean and the results are shown in Fig. 5(b) and (ii). This figure clearly shows the presence of wave activities in both intensity and wind observations and these have larger amplitudes in the SE, SW and ZEN directions, particularly for the intensities. Lomb-Scargle analysis of the intensity and wind perturbations yields periodograms presented in Fig. 5(c) and (iii), respectively. For the intensity periodogram (refer to Fig. 5(c)), the most dominant periods (i.e. highest power

that is above 75% confidence level) are approximately 107 and 56 min in the SW look direction, and 57 min in the SE look direction. The power in the wind periodogram (see Fig. 5(iii)) shows a single peak at periods of 54 and 52 min in the SW and NE look directions respectively, while multiple peaks with a period range of 45–142 min are observed for the SE and ZEN look directions (i.e. SE peaks at 59, 95 and 142 min and ZEN at 39 and 45 min). Note that there are large data gaps in the zenith, north-east and north-west look directions, and therefore period decomposition in those look directions is deemed not reliable. Also, periods larger than 180 min (3 h) are ignored as they are greater than half the data length used to produce the periodogram and therefore are under sampled. It is noted that the majority of the dominant periods detected from this FPI data are similar to those detected from the GPS TEC data, but the FPI also observed larger periods than those from the TEC data. Propagation characteristics of the waves observed with the FPI could not be determined due to the fact that the average time delays between the SE and SW look directions (the only directions with significant data for this task) are almost zero. This means that the data sampling (~9 min) is too coarse/sparse and thus results in failure to resolve the wave's zonal velocity component.

Analysis of the all-sky camera keogram, presented in Fig. 6(a), during the night of 6 January 2014 shows intensity brightening that stretched across the field of view at around 18 UT, which coincides with TID/AGW observations from GPS and FPI measurements. Fig. 6(b) shows intensities extracted at latitudes closest to the GPS stations (i.e. 75.25°, 76.58° and 78.15°) between 1730 and 1930 UT for wave period and propagation analysis. A shift in peaks at around 18 UT is observed from this figure; the peak is first observed at the southern-most latitude (i.e. 75.25°, blue curve) and last in the northern-most latitude (i.e. 78.15°, black curve). This suggests that the auroral structure is propagating in a poleward direction. Using time delays between peaks at different latitudes and the distance between observation points, we estimate a virtual horizontal velocity of $\sim 823 \pm 143$ m/s. Fig. 6(c) presents periodograms of the results presented in (b). The dominating periods were found to be ~60 min for observations at 75.25° as well as 76.58°, and ~97 min for observations at 78.15°. It is worth noting that these properties were obtained by assuming that the 557.7 nm airglow altitude is roughly 110 km. These wave periods and velocity are in agreement with those obtained for the wave-like structures observed from the GPS TEC and FPI measurements.

Fig. 7(a) shows geomagnetic X-component measurements between 1730 and 1930 UT, while (b) shows the same but with the baseline removed. Measurements for Fig. 7(b) were obtained from SuperMAG (supermag.jhuapl.edu/mag), where the baseline was calculated from the yearly trend in order to retain only the currents flowing in and between the ionosphere and magnetosphere (Gjerloev, 2012). A magnetic disturbance is seen at around

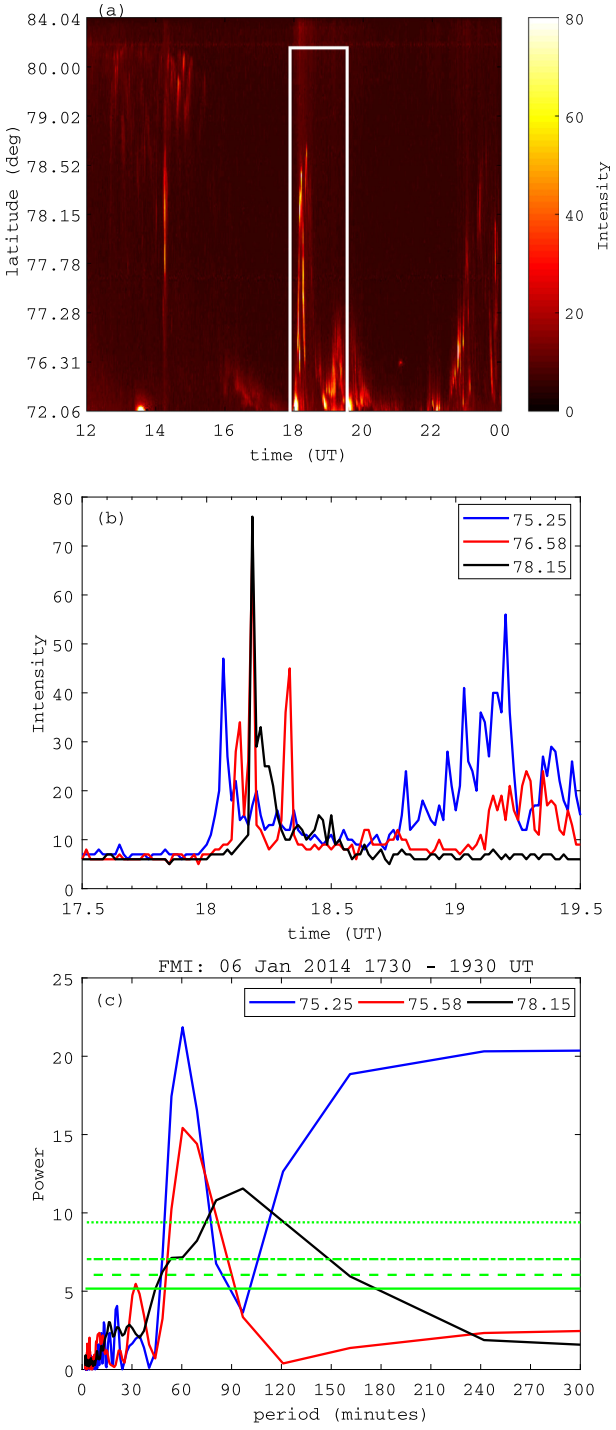

Fig. 6. (a) Keogram from the all-sky camera in Longyearbyen on 6 January 2014. (b) Intensities of 557 nm wavelength between 1730 and 1930 UT on 6 January 2014 at different latitudes (75.25°, blue; 76.58°, red; 78.15°, black) as well as their corresponding periodograms (c). Note that the white box in (a) highlights the auroral activity of interest while green horizontal lines in (c) show the same confidence levels as in Fig. 4. (For interpretation of the references to colour in this figure legend, the reader is referred to the web version of this article.)

18 UT in all three stations but at different times. To determine whether this disturbance may be the source of or linked to the wave-like structures seen in the GPS, FPI,

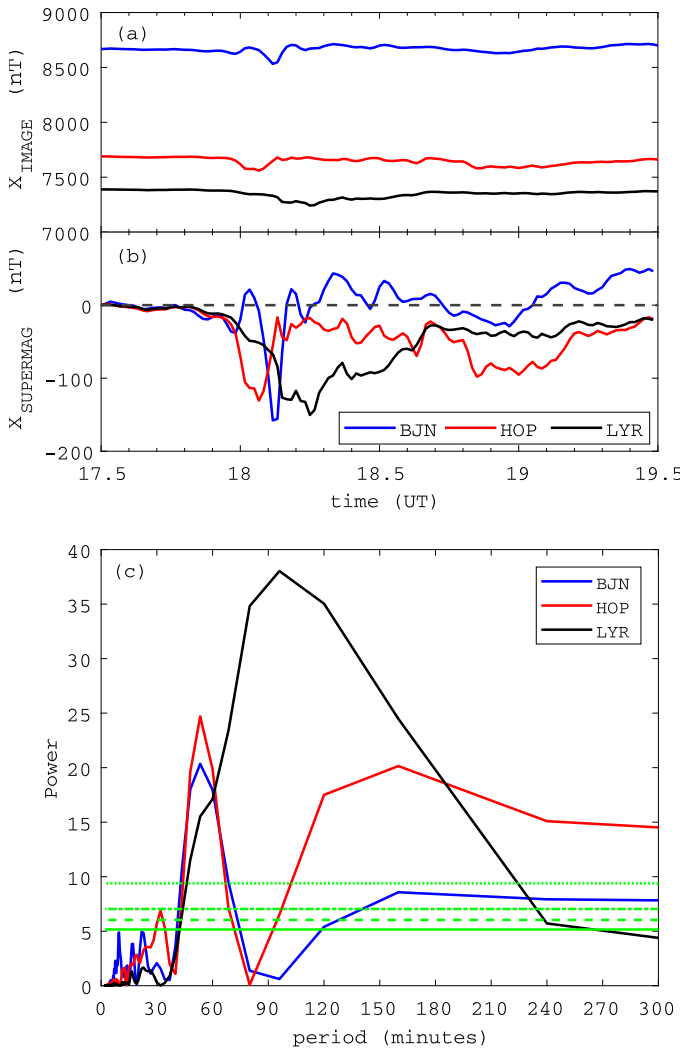

Fig. 7. (a) Geomagnetic X-component, (b) X-component with baseline removed and (c) corresponding periodograms. The black dashed line in (b) show the zero $X_{SUPERMAG}$ value and the green horizontal lines in (c) show the same confidence levels as in Fig. 4. (For interpretation of the references to colour in this figure legend, the reader is referred to the web version of this article.)

and all-sky camera measurements, Lomb-Scargle frequency analysis and SADM-GPS methods were applied to the data in order to extract period and propagation information. Note that we used SADM-GPS since the geometry of magnetometers is the same as the GNSS stations (i.e. magnetometers are co-located with GNSS receivers), but with IPP velocities set to zero since the measurements are stationary. The periodograms reveal that the primary period is approximately 53 min for BJN and HOP observatories, and a secondary period of 32 min for HOP. Note again that periods larger than 60 min are ignored (for example 96 min for LYR station) since these periods are greater than half the data length. The horizontal velocity and azimuth are estimated as $\sim 708 \pm 261$ m/s and $\sim 2^{\circ} \pm 29^{\circ}$ (i.e. poleward propagation), respectively. Again, these wave properties seems to agree with those obtained from GPS TEC and the all-sky camera.

4. Discussions

All the characteristics of AGWs/TIDs determined from the different instruments used in this study are summarised in Table 3. The periods and velocities are comparable to previous studies conducted at high latitudes; for example a study by Nicolls et al. (2012) observed gravity waves with a period of 32 ± 0.2 min, horizontal phase speed of 350–770 m/s and propagation direction of 17°–50° (i.e. poleward direction) during quiet conditions on 9–10 January 2010 in Alaska. Similarly, Momani et al. (2010) reported on large-scale TIDs propagating polewards at 800–1200 m/s and 300–400 m/s over Antarctica during storms in October and November 2003, respectively. Also, Ford et al. (2006) observed poleward propagating large-scale AGWs with a period of 1.8 h and horizontal velocity of 250 m/s in northern Scandinavia, which they linked to Joule heating from electrojet activity. Studies by Hajkowicz and Hunsucker (1987), Yeh et al. (1994), Tsugawa et al. (2003), Lee et al. (2004), Tsugawa et al. (2004), Bruinsma and Forbes (2007), Borries et al. (2009), Pradipta et al. (2016), Figueiredo et al. (2017) have also reported similar results to those presented in this paper, for disturbances linked to storm/substorm activity. The speeds are higher than some obtained from AGWs/TIDs of auroral origins observed at lower latitudes, e.g. Afraimovich et al. (2000), Ding et al. (2008), Habarulema et al. (2013), but this is expected as ion drag may reduce the speeds far from the source (Balthazor and Moffet, 1999).

Although a small substorm is observed around 18 UT, i.e. the AE index in Fig. 2 only reaches a maximum of around 200 nT, the all-sky camera frames in Fig. 8 clearly show evidence of auroral activity. This substorm/auroral activity correlates to the time of observations of AGWs/TIDs from ionospheric and thermospheric measurements. Also Fig. 8 shows that the auroral arc is first seen south of the observing station (see Fig. 8(a)) and quickly progresses north towards the station (see Fig. 8(b–d)). This confirms a poleward propagation as was estimated from the keogram results in Fig. 6, since both results represent the same observation but in a slightly different way. The poleward propagation direction is also in agreement, in general, with observations obtained from TEC and mag-

Table 3
Summary of the wave characteristics calculated from different instruments. Note that the period and Vh columns show the minimum and maximum values determined for each instrument are given (if these parameters couldn't be determine, a dash (i.e. "–") is shown instead), directions are given in N, NE, NW which denotes north, north-east, and north-west respectively.

Instrument	Period (min)	Vh (m/s)	Direction
GNSS/GPS	18–65	749–761	N-NW
FPI	42–142	–	–
ASC	60–97	823	N
Magnetometer	32–53	708	N-NE

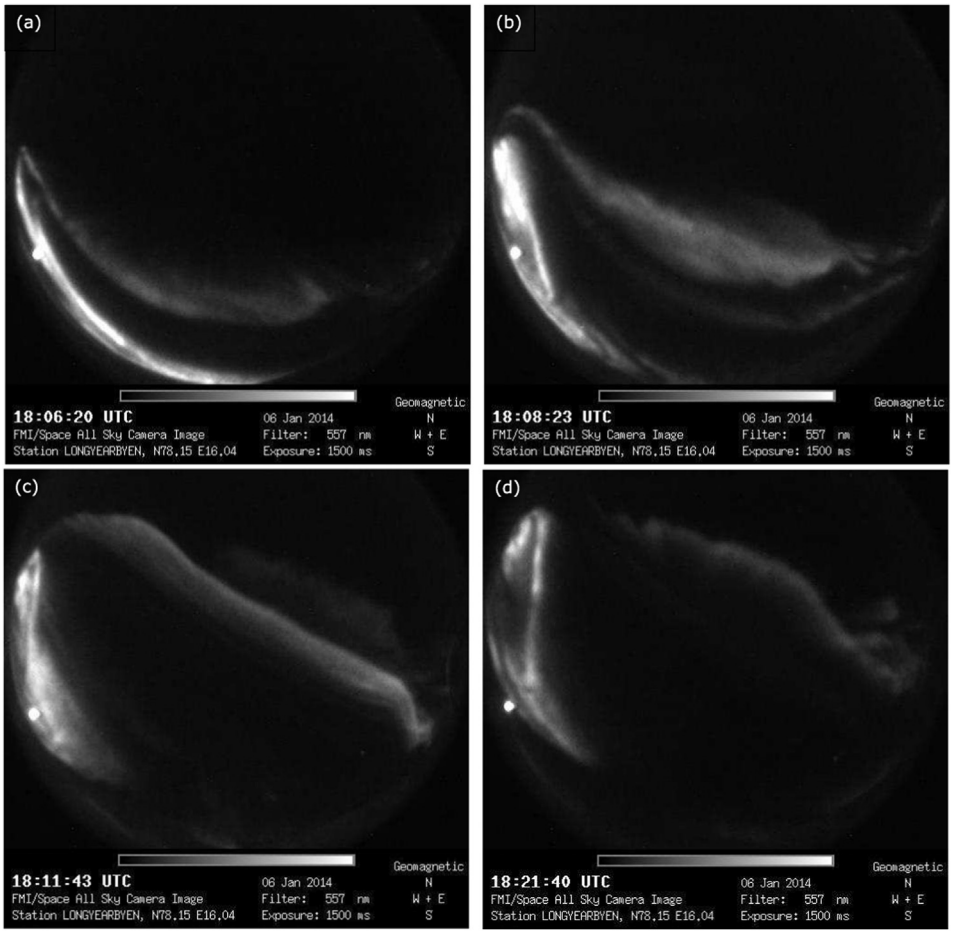

Fig. 8. All-sky camera frames between 18:06 and 18:22 UT showing auroral activity at 557 nm.

netic field measurements (i.e. mean azimuths of roughly 345° and 2°, respectively).

A correlation of periods, horizontal velocities and azimuths of the wave structures detected from TEC, intensity and magnetic field measurements indicates that these disturbances are related, although the measurements sample different heights of the ionosphere/thermosphere. For example, TEC measurements were calculated assuming a thin shell at ~300 km (corresponding to typical height of the maximum electron density in the F-region), while the all-sky camera estimates the 557.7 nm airglow emission at ~110 km and X-magnetic field deflections infers about ionospheric currents at this same height. A study by Shiokawa et al. (2003) also reported similar velocities for their observed AGW/TIDs sampled at different altitudes using 630 nm airglow, TEC and virtual height measurements from an all-sky airglow imager, GPS, and ionosonde; they obtained velocities of 640 m/s from the all-sky imager, 370–560 m/s from GPS and 580 m/s from the ionosondes. However that study was based on measurements taken in the low-middle latitudes, whereas this study used measurements from the Arctic polar cap.

Previous investigations have indicated that the sources of large-scale TIDs in the polar regions are particle precipitation, Joule heating and Lorentz forcing (e.g. Chimona and Hines, 1970; Davis, 1971; Hunsucker, 1982; Hajkowicz and Hunsucker, 1987). These mechanisms result from the magnetosphere becoming intermittently unstable under the influence of the solar wind and depositing large amounts of energy into the polar upper atmosphere (Davis, 1971). It is not possible to quantify Joule heating, particle precipitation or Lorentz forcing because the intensity measurements from the all-sky camera are not calibrated and there are no electric field measurements from a nearby EISCAT radar for this case. However, the fact that an aurora was observed at the similar time as the AGWs/TIDs, as shown by the keogram in Fig. 6, as well the all-sky camera images presented in Fig. 8, indicates that there was particle precipitation. Also, past studies have shown that the Joule heating, Lorentz forcing and particle precipitation are statistically linearly related to the AE index (Ahn et al., 1983; Wei et al., 1985), which is obtained from the horizontal magnetic field. The results presented here show similar periods for the TEC, auroral intensity and the horizontal magnetic field X-component. Rice et al. (1988) studied AGW generation and propagation for a moderate geomagnetic activity event on 18 October 1985 and reported that the observed AGWs had comparable periods to the temporal separation of two substorms that occurred near the general source region. Also, a study

on the generation, propagation and dissipation of AGWs over the European sector between 1985 and 1990 by Williams et al. (1993) found that EISCAT electric field measurements showed similar periodic modulation to the HF Doppler measurements from which gravity waves were observed. These studies showed that the TIDs and associated auroral sources may have similar periodicities, as has been observed by this study. Therefore it is likely that Joule heating or/and particle precipitation as a result of auroral energy injection are probable generation mechanisms for the observed AGWs/TIDs.

5. Conclusion

This paper presented observations of AGW/TIDs from ionospheric radio (i.e. GNSS) and thermospheric optical (i.e. FPI) measurements over Svalbard. The periods of these disturbances varied between 18 and 142 min with the larger periods obtained from the FPI measurements. In addition the wave-like structures were found to propagate in a poleward direction with mean speeds of ~749–761 m/s. At the same time of AGWs/TIDs observations, disturbances in magnetometer and all-sky camera measurements in the vicinity of the AGWs/TIDs were also observed. The periods and propagation velocities of these disturbances corresponded to those of the TIDs/AGWs. This led to the conclusion that the AGWs/TIDs were probably generated by Joule heating or/and particle precipitation related to the observed auroral activity. Although the amount of Joule heating or particle precipitation could not be calculated due to lack of electric field estimates from the co-located EISCAT radar, the electric field could be estimated from nearby SuperDARN (Super Dual Auroral Radar network) radars in future. To the best of the authors' knowledge, this study shows the first correlation of period and propagation properties of large-scale AGWs/TIDs using radio, optical and magnetic field measurements in the Arctic polar cap.

Acknowledgments

For the ground magnetometer data from SuperMAG we gratefully acknowledge SuperMAG PI Jesper W. Gjerloev; the institutes who maintain the IMAGE magnetometer array, PI Liisa Juusola; the Tromsø Geophysical Obervatory at the University of Tromsø for operation for the three magnetometers used in this study (i.e. BJN, HOP, and LYR).

ZTKJ and ALA were supported by the Royal Society's Newton Advanced Fellowship Grant NA150012. Also, KO acknowledges financial support from the Norwegian Research Council under contracts 212014 and 223252.

References

Afraimovich, E., Astafyeva, E., Demyanov, V., Edemskiy, I., Gavrilyuk, N., Ishin, A., Kosogorov, E., Leonovich, L., Lesyuta, O., Palamartchouk, K., Perevalova, N., Polyakova, A., Smolkov, G., Voeykov, S., Yasyukevich, Y., Zhivetiev, I., 2013. A review of GPS/GLONASS studies of the ionospheric response to natural and anthropogenic processes and phenomena. J. Space Weather Space Clim. 3, A27. https://doi.org/10.1051/swsc/2013049.

Afraimovich, E., Kosogorov, E., Leonovich, L., Palamartchouk, K., Perevalova, N., Pirog, O., 2000. Determining parameters of large-scale traveling ionospheric disturbances of auroral origin using GPS-arrays. J. Atmos. Sol. Terr. Phys. 62, 553–565. https://doi.org/10.1016/S1364-6826(00)00011-0.

Afraimovich, E., Palamartchouk, K., Perevalova, N., 1998. GPS radio interferometry of travelling ionospheric disturbances. J. Atmos. Sol. Terr. Phys. 60, 1205–1223. https://doi.org/10.1016/S-1364-6826(98)00074-1.

Ahn, B.H., Akasofu, S.I., Kamide, Y., 1983. The Joule heat production rate and the particle energy injection rate as a function of the geomagnetic indices AE and AL. J. Geophys. Res. 88, 6275–6287. https://doi.org/10.1029/JA088iA08p06275.

Aruliah, A., Griffin, E., 2001. Evidence of meso-scale structure in the high-latitude thermosphere. Ann. Geophys. 19, 37–46. https://doi.org/10.5194/angeo-19-37-2001.

Balachandran, N., 1980. Gravity waves from thunderstorms. Mon. Weather Rev. 108, 804–816. https://doi.org/10.1175/1520-0493(1980)108<0804:GWFT>2.0.CO;2.

Balthazor, R., Moffet, R., 1999. Morphology of large-scale traveling atmospheric disturbances in the polar thermosphere. J. Geophys. Res. 104, 15–24. https://doi.org/10.1029/1998JA900039.

Becker, E., Vadas, S., 2018. Secondary gravity waves in the winter mesosphere: Results from a high-resolution global circulation model. J. Geophys. Res. Atmos. 123, 2605–2627. https://doi.org/10.1002/2017JD027460.

Borries, C., Jakowski, N., Wilken, V., 2009. Storm-induced large scale TIDs observed in GPS derived TEC. Ann. Geophys. 27, 1605–1612. https://doi.org/10.5194/angeo-27-1605-2009.

Borries, C., Mahrous, A., Ellahouny, N., Badeke, R., 2016. Multiple ionospheric perturbations during the Saint Patrick's Day storm 2015 in the European-African sector. J. Geophys. Res. Space Phys. 121, 11333–11345. https://doi.org/10.1002/2016JA023178.

Bruinsma, S., Forbes, J., 2007. Global observation of traveling atmospheric disturbances (TADs) in the thermosphere. Geophys. Res. Lett. 34, L14103. https://doi.org/10.1029/2007GL030243.

Cai, H., Yin, F., Ma, S., McCrea, I., 2011. Observations of AGW/TID propagation across the polar cap: a case study. Ann. Geophys. 29, 1355–1363. https://doi.org/10.5195/angeo-29-1355-2011.

Chan, K., Villard Jr., O., 1962. Observations of large-scale traveling ionospheric disturbances by spaced-path high-frequency instantaneous-frequency measurements. J. Geosphy. Res. 67, 973–988. https://doi.org/10.1029/JZ067i003p00973.

Chimona, G., Hines, C., 1970. Atmospheric gravity waves launched by auroral currents. Planet. Space Sci. 18, 565–582. https://doi.org/10.1016/0032-0633(70)90132-7.

Datta-Barua, S., Lee, J., Pullen, S., Luo, M., Ene, A., Zhang, G., Enge, P., 2010. Ionospheric threat parameterization for local area Global-Positioning-System-based aircraft landing systeyms. J. Aircraft 47, 1141–1151. https://doi.org/10.2514/1.46719.

Davis, M., 1971. On polar substorms as the source of large-scale traveling ionospheric disturbances. J. Geophys. Res. 76, 4525–4533. https://doi.org/10.1029/JA076i019p04525.

Davis, T., Sugiura, M., 1966. Auroral electrojet activity index AE and its universal time variations. J. Geophys. Res. 71, 785–801. https://doi.org/10.1029/JZ071i003p00785.

Ding, F., Wan, W., Ning, B., Wang, M., 2007. Large-scale traveling ionspheric disturbances observed by GPS total electron content during the magnetic storm of 29-30 October 2003. J. Geophys. Res., 112 https://doi.org/10.1029/2006JA012013.

Ding, R., Wan, W., Liu, L., Afraimovich, E., Voeykov, S., Perevalova, N., 2008. A statistical study of large-scale traveling ionospheric disturbances observed by GPS TEC during major magnetic storms over the

years 2003-2005. J. Geophys. Res. 113, A00A01. https://doi.org/10.1029/2008JA013037.
Figueiredo, C., Wrasse, C., Takahashi, H., Otsuka, Y., Shiokawa, K., Barros, D., 2017. Large-scale traveling ionospheric disturbances observed by GPS dTEC maps over North and South America on Saint Patrick's Day storm in 2015. J. Geophys. Res. Space Phys. 122, 4755–4763. https://doi.org/10.1002/2016JA023417.
Figueiredo, C.A.O.B., Takahashi, H., Wrasse, C.M., Otsuka, Y., Shiokawa, K., Barros, D., 2018. Medium-scale traveling ionospheric disturbances observed by detrended total electron content maps over Brazil. J. Geophys. Res. Space Phys. 123, 2215–2227. https://doi.org/10.1002/2017JA025021.
Ford, E., Aruliah, A., Griffin, E., McWhirter, I., 2006. Thermospheric gravity waves in Fabry-Perot Interferometer measurements of the 630.0 mn OI line. Ann. Geophys. 24, 555–566. https://doi.org/10.5194/angeo-24-555-2006.
Ford, E., Aruliah, A., Griffin, E., McWhirter, I., 2008. Statistical analysis of thermospheric gravity waves from Fabry-Perot Interferometer measurements of atomic oxygen. Ann. Geophys. 26, 29–45. https://doi.org/10.5194/angeo-26-29-2008.
Fovell, R., Durran, D., Holton, J., 1992. Numerical simulations of convectively generated stratospheric gravity waves. J. Atmos. Sci 49, 1427–1442. https://doi.org/10.1175/1520-0469(1992)049<1427:NSOCGS>2.0.CO;2.
Fritts, D., Nastrom, G., 1992. Sources of mesoscale variability of gravity waves. Part II: Frontal, convective and jet stream excitation. J. Atmos. Sci. 49, 111–127. https://doi.org/10.1175/1520-0469(1992)049<0111:SOMVOG>2.0CO;2.
Gall, R., Williams, R., Clark, T., 1988. Gravity waves generated during frontogenesis. J. Atmos. Sci. 45, 2204–2219. https://doi.org/10.1175/1520-0469(1988)045<2204:GWGDF>2.0CO;2.
Gjerloev, J., 2012. The SuperMAG data processing technique. J. Geophys. Res 117, A09213. https://doi.org/10.1029/2012JA017683.
Guo, J., Liu, H., Feng, X., Pulkkinen, T.I., Tanskanen, E.I., Liu, C., Zhong, D., Wang, Y., 2014. MLT and seasonal dependence of auroral electrojets: IMAGE magnetometer network observations. J. Geophys. Res. Space Phys. 119, 3179–3188. https://doi.org/10.1002/2014JA019843.
Habarulema, J., Katamzi, Z., McKinnell, L.A., 2013. Estimating the propagation characteristics of large-scale traveling ionospheric disturbances using ground-based and satellite data. J. Geophys. Res. Space Phys. 118, 7768–7782. https://doi.org/10.1002/2013JA018997.
Habarulema, J., Katamzi, Z., Yizengaw, E., 2015. First observations of poleward large-scale traveling ionospheric disturbances over the African sector during geomagnetic storms. J. Geophys. Res. Space Phys., 120 https://doi.org/10.1002/2015JA021066.
Habarulema, J., Katamzi, Z., Yizengaw, E., Yamazaki, Y., Seemala, G., 2016. Simultaneous storm time equatorward and poleward large-scale TIDs on a global scale. Geophys. Res. Lett. 43, 6678–6686. https://doi.org/10.1002/2016GL069740.
Habarulema, J., Yizengaw, E., Katamzi-Joseph, Z., Moldwin, M., Buchert, B., 2018. Storm time global observations of large-scale TIDs from ground-based and in situ satellite measurements. J. Geophys. Res. Space Phys. 123, 711–724. https://doi.org/10.1002/2017JA024510.
Hajkowicz, L., 1990. A global study of large scale traveling ionospheric disturbances (TIDs) following a step-like onset of auroral substorms in both hemisphere. Planet. Space Sci. 38, 913–923. https://doi.org/10.1016/0032-0633(90)90058-X.
Hajkowicz, L., Hunsucker, R., 1987. A simultaneous observation of large-scale periodic TIDs in both hemispheres following an onset of auroral disturbances. Planet. Space Sci. 35, 785–791. https://doi.org/10.1016/0032-0633(87)90038-9.
Hayashi, H., Nishitani, N., Ogawa, T., Otsuka, Y., Tsugawa, T., Hosokava, K., Saito, A., 2010. Large-scale traveling ionospheric disturbances observed by SuperDARN Hokkaido HF radar and GPS network on 15 December 2006. J. Geophys. Res. 115, A06309. https://doi.org/10.1029/2009JA014297.
Hernàndez-Parajes, Juan, J., Sanz, J., 2006. Medium-scale traveling ionospheric disturbances affecting GPS measurements: Spatial and temporal analysis. J. Geophys. Res., 111 https://doi.org/10.1029/2005JA011474.
Hines, C., 1960. Internal atmospheric gravity waves at ionospheric heights. Can. J. Phys. 38, 1441–1481. https://doi.org/10.1139/p60-150.
Hocke, K., Schlegel, K., 1996. A review of atmospheric gravity waves and travelling ionospheric disturbances: 1982-1995. Ann. Geophys. 14, 917–940. https://doi.org/10.1007/s00585-996-0917-6.
Hunsucker, R., 1982. Atmospheric gravity waves generated in the high-latitude ionosphere: A review. J. Geophys. Res. 20, 293–315. https://doi.org/10.1029/RG020i002p00293.
Idrus, I.I., Abdullah, M., Hasbi, A.M., Husin, A., Yatim, B., 2013. Large-scale traveling ionospheric disturbances observed using GPS receivers over high-latitude and equatorial regions. J. Atmos. Sol. Terr. Phys. 102, 321–328. https://doi.org/10.1016/j.astp.2013.06.014.
Innis, J., Greet, P., Dyson, P., 2001. Evidence for thermospheric gravity waves in the southern polar cap from ground-based vertical velocity and photometric observations. Ann. Geophys. 19, 533–543. https://doi.org/10.5195/angeo-19-533-2001.
Johnson, F., Hanson, W., Hodges, R., Coley, W., Carignan, G., Spencer, N., 1995. Gravity waves near 300 km over the polar caps. J. Geophys. Res., 100 https://doi.org/10.1029/95JA02858.
Katamzi, Z., Habarulema, J., 2014. Traveling ionospheric disturbances observed at South African midlatitudes during the 29-31 October 2003 geomagnetically disturbed period. Adv. Space. Res. 53, 48–62. https://doi.org/10.1016/j.asr.2013.10.019.
Kotake, N., Otsuka, Y., Ogawa, T., Tsugawa, T., Saito, A., 2007. Statistical study of medium-scale traveling ionospheric disturbances observed with the GPS networks in Southern California. Earth Planets Space 59, 95–102. https://doi.org/10.1186/BF03352681.
Lee, C.C., Liu, J.Y., Chen, M.Q., Su, S.Y., Yeh, H.C., Nozaki, K., 2004. Observation and model comparisons of the traveling atmospheric disturbances over the Western Pacific region during the 6-7 April 2000 magnetic storm. J. Geophys. Res. 109, A09309. https://doi.org/10.1029/2003JA010267.
Lomb, N., 1976. Least-squares frequency analysis of unequally spaced data. Astrophys. Space Sci. 39, 447–462. https://doi.org/10.1007/BF00648343.
MacDougall, J., Hall, G., Hayashi, K., 1997. F region gravity waves in the central polar cap. J. Geophys. Res. 102, 14513–14530. https://doi.org/10.1029/97JA01076.
Matsuda, T.S., Nakamura, T., Ejiri, M.K., Tsutsumi, M., Tomikawa, Y., Taylor, M.J., Zhao, Y., Pautet, P.D., Murphy, D.J., Moffat-Griffin, T., 2017. Characteristics of mesospheric gravity waves over Antarctica observed by Antarctic Gravity Wave Instrument Network imagers using 3-D spectral analyses. J. Geophys. Res. Atmos. 122, 8969–8981. https://doi.org/10.1002/2016JD026217.
Mayr, H., Harris, I., Varisi, F., Herrero, F., 1984. Global excitation of wave phenomena in a dissipative multiconstituent medium: 1 Transfer function of the Earth's thermosphere. J. Geophys. Res. 89, 10929–10959. https://doi.org/10.1029/JA089iA12p10929.
van der Meeren, C., Oksavik, K., Lorentzen, D., Paxton, L., Clausen, L., 2016. Scintillation and irregularities from the nightside part of a Sun-aligned polar cap arc. J. Geophys. Res. Space Phys. 121, 5723–5736. https://doi.org/10.1002/2016JA022708.
van der Meeren, C., Oksavik, K., Lorentzen, D., Rietveld, M., Clausen, L., 2015. Severe and localized GNSS scintillation at the poleward edge of the nightside auroral oval during intense substorm aurora. J. Geophys. Res. Space Phys. 120, 10607–10621. https://doi.org/10.1002/2015JA021819.
Momani, M., Yatim, B., Ali, M., 2010. Large-scale traveling ionospheric disturbances observed by GPS receivers in Antarctica. Wuhan Univ. J. Nat. Sci. 15, 135–142. https://doi.org/10.1007/s11859-010-0210-0.
Ngwira, C., McKinnell, L.A., Cilliers, P., Yizengaw, E., 2012. An investigation of ionospheric disturbances over South Africa during the magnetic storm on 15 May 2005. Adv Space Sci. 49, 327–335. https://doi.org/10.1016/j.asr.2011.09.035.

Nicolls, M., Vadas, S., Meriwether, J., Conde, M., Hampton, D., 2012. The phases and amplitudes of gravity waves propagating and dissipating in the thermosphere. J. Geophys. Res. 117, A05323. https://doi.org/10.1029/2012JA017542.

Nishioka, M., Saito, A., Tsugawa, T., 2009. Super-medium-scale traveling ionospheric disturbance observed at midlatitude during the geomagnetic storm on 10 November 2004. J. Geophys. Res. 114, A07310. https://doi.org/10.1029/2008JA013581.

NovAtel Inc., 2012. GPStation-6 GNSS ionosphere scintillation and TEC monitor (GITSM) receiver user manual. Calgary, Alberta. [Available at http://www.novatel.com/assets/Documents/Manuals/om-20000121.pdf, Accessed date 29 Mar. 2018].

Oksavik, K., van der Meeren, C., Lorentzen, D., Baddeley, L., Moen, J., 2015. Scintillation and loss of signal lock from poleward moving auroral forms in the cusp ionosphere. J. Geophys. Res. Space Phys. 120, 9161–9175. https://doi.org/10.1002/2015JA021528.

Otsuka, Y., Suzuki, K., Nakagawa, S., Nishioka, M., Shiokawa, K., Tsugawa, T., 2013. GPS observations of medium-scale traveling ionospheric disturbances over Europe. Ann. Geophys. 31, 163–172. https://doi.org/10.5194/angeo-31-163-2013.

Pi, X., Mendillo, M., Hughes, W., Buonsanto, M., Sipler, D., Kelly, J., Zhou, Q., Lu, G., Hugh, T., 2000. Dynamical effects of geomagnetic storms and substorms in the middle-latitude ionosphere: An observational campaign. J. Geophys. Res. 105, 7403–7417,. https://doi.org/10.1029/1999JA900460.

Pradipta, R., Valladares, C.E., Carter, B.A., Doherty, P.H., 2016. Interhemispheric propagation and interactions of auroral traveling ionospheric disturbances near the equator. J. Geophys. Res. Space Phys. 121, 2462–2474. https://doi.org/10.1002/2015JA022043.

Rees, D., Smith, R., Charleton, P., McCormac, F., Lloyd, N., Steen, A., 1984. The generation of vertical thermospheric winds and gravity waves at auroral latitudes - I. Observations of vertical winds. Planet. Space Sci. 32, 667–684. https://doi.org/10.1016/0032-0633(84)90092-8.

Rice, D., Hunsucker, R., Lanzerotti, L., Crowley, G., Williams, P., Craven, J., Frank, L., 1988. An observation of atmospheric gravity wave cause and effect during the October 1995 WAGS campaign. Radio Sci. 23, 919–930. https://doi.org/10.1029/RS023i006p00919.

Sangalli, L., Partamies, N., Syrjäsuo, M., Enell, S.F., Kauristie, K., Mäkinen, S., 2011. Performance study of the new EMCCD-based all-sky cameras for auroral imaging. Int. J. Remote Sens. 32, 2987–3003. https://doi.org/10.1080/0143111.2010.541505.

Satomura, T., Sato, K., 1999. Secondary generation of gravity waves associated with the breaking of mountain waves. J. Atmos. Sci. 56, 3847–3858. https://doi.org/10.1175/1520-0469(1999)056<3847:SGOGWA>2.0.CO;2.

Scargle, J., 1982. Studies in astronomical time series analysis: II Statistical aspects of spectral analysis of unevenly space data. Astrophys. J. 263, 835–853. https://doi.org/10.1086/160554.

Shiokawa, K., Mori, M., Otsuka, Y., Oyama, S., Nozawa, S., 2012. Motion of high-latitude nighttime medium-scale traveling ionospheric disturbances associated with auroral brightening. J. Geophys. Res. 117, A10316. https://doi.org/10.1029/2012JA017928.

Shiokawa, K., Otsuka, Y., Balan, N., Igarashi, K., Ridley, A., Knipp, D., Saito, A., Yumoto, K., 2002. A large-scale traveling ionospheric disturbance during the magnetic storm of 15 September 1999. J. Geophys. Res. 107, 1088. https://doi.org/10.1029/2001JA000245.

Shiokawa, K., Otsuka, Y., Ogawa, T., Kawamura, S., Yamamoto, M., Fukao, S., Nakamura, T., Tsuda, T., Balan, N., Igarashi, K., Lu, G., Saito, A., Yumoto, K., 2003. Thermospheric wind during a storm-time large-scale traveling ionospheric disturbance. J. Geophys. Res. 108, 1423. https://doi.org/10.1029/2003JA010001.

Stauning, P., 2013. The polar cap index: A critical review of methods and a new approach. J. Geophys. Res. Space Sci. 118, 5021–5030. https://doi.org/10.1002/jgra.50462.

Takahashi, H., Wrasse, C., Figueiredo, C., Barros, D., Abdu, M., Otsuka, Y., Shiokawa, K., 2018. Equatorial plasma bubble seeding by MSTIDs in the ionosphere. Progress Earth Planet. Sci. 5. https://doi.org/10.1186/s40645-018-0189-2.

Taylor, M., Hapgood, M., 1988. Identification of a thunderstorm as a source of short period gravity waves in the upper atmospheric nightglow emissions. Planet. Space Sci. 36, 975–985. https://doi.org/10.1016/0032-0633(88)90035-9.

Troshichev, O., Andrezen, V., 1985. The relationship between interplanetary quantities and magnetic activity in the southern polar cap. Planet. Space Sci. 33, 415–419. https://doi.org/10.1016/0032-0633(85)90086-8.

Tsugawa, T., Saito, A., Otsuka, Y., 2004. A statistical study of large-scale traveling ionospheric disturbances using the GPS network in Japan. J. Geophys. Res. 109, A06302. https://doi.org/10.1029/2003JA010302.

Tsugawa, T., Saito, A., Otsuka, Y., Yamamoto, M., 2003. Damping of large-scale traveling ionospheric disturbances detected with GPS networks during the geomagnetic storm. J. Geophys. Res. 108, 1127. https://doi.org/10.1029/2002JA009433.

Vaasiliadis, D., Angelopoulos, V., Baker, D., Klimas, A., 1996. The relation between the northern polar cap and auroral electrojet geomagnetic indices in wintertime. Geophys. Res. Lett. 23, 2781–2784. https://doi.org/10.1029/96GL02575.

Vadas, S., Liu, H., 2009. Generation of large-scale gravity waves and neutral winds in the thermosphere from the dissipation of convectively generated gravity waves. J. Geophys. Res. 114, A10310. https://doi.org/10.1029/2009JA014108.

Vadas, S., Zhao, J., Chu, X., Becker, E., 2018. The excitation of secondary gravity waves from body forces: Theory and observation. J. Geophys. Res. Atmos. https://doi.org/10.1029/2017JD027970.

Valladares, C., Hei, M., 2012. Measurements of the characteristics of TIDs using small and regional networks of GPS receivers during the campaign of 17-30 July of 2008. Int. J. Geophys. https://doi.org/10.1155/2012/548784.

Valladares, C., Villalobos, J., Hei, M., Sheehan, R., Basu, S., MacKenzie, E., Doherty, P., Rios, V., 2009. Simultaneous observations of traveling ionospheric disturbances in the Northern and Southern Hemispheres. Ann. Geophys. 27, 1501–1508. https://doi.org/10.5194/angeo-27-1501-2009.

Vennerstrøm, S., Friis-Christensen, E., Troshichev, O., Andresen, V., 1991. Comparison between the polar cap index, PC, and the auroral electrojet indices AE, AL, and AU. J. Geophys. Res. 96, 101–113. https://doi.org/10.1029/90JA01975.

Viereck, R., Deehr, C., 1989. On the interaction between gravity waves and the OH Meinel(6-2) and the O_2 atmospheric (0-1) bands in the polar night airglow. J. Geophys. Res. 94, 5397–5404. https://doi.org/10.1029/JA094iA05p05397.

Vlasov, A., Kauristie, K., Kamp, M.V.D., Luntama, J.P., 2011. A study of traveling ionospheric disturbances and atmospheric gravity waves using EISCAT Svalbard IPY-data. Ann. Geophys. 29, 2101–2116. https://doi.org/10.5194/angeo-29-2101-2011.

Wei, S., Ahn, B.H., Akasofu, S.I., 1985. The global Joule heat production rate and the AE index. Planet. Space Sci. 33, 271–279. https://doi.org/10.1016/0032-0633(85)90059-5.

Williams, P., Virdi, T., Lewis, R., Lester, M., Rodger, A., McCrea, I., Freeman, K., 1993. Worldwide atmospheric gravity-wave study in the European sector 1985-1990. J. Atmos. Terr. Phys. 55, 683–696. https://doi.org/10.1016/0021-9169(93)90014-P.

Yeh, K., Ma, S., Lin, K., Conkright, R., 1994. Global ionospheric effects of the October 1989 geomagnetic storm. J. Geophys. Res. 99, 6201–6218. https://doi.org/10.1029/93JA02543.

Yoon, M., Lee, J., 2014. Medium-scale traveling ionospheric disturbances in the Korean region on 10 November 2004: Potential impact on GPS-based navigation systems. Space Weather 12, 173–186. https://doi.org/10.1002/2013SW001002.

Zakharenkova, I., Astafyeva, E., Cherniak, I., 2016. GPS and GLONASS observations of large-scale traveling ionospheric disturbances during the 2015 St. Patrick's Day storm. J. Geophys. Res. Space Phys. 121, 12138–12156. https://doi.org/10.1002/2016JA023332.